NBR1 enables autophagy-dependent focal adhesion turnover

Candia M. Kenific,[1,3] Samantha J. Stehbens,[2] Juliet Goldsmith,[1,3] Andrew M. Leidal,[1] Nathalie Faure,[1] Jordan Ye,[1] Torsten Wittmann,[2] and Jayanta Debnath[1]

[1]Department of Pathology and Helen Diller Family Comprehensive Cancer Center, [2]Department of Cell and Tissue Biology, and [3]Biomedical Sciences Graduate Program, University of California, San Francisco, San Francisco, CA 94143

Autophagy is a catabolic pathway involving the sequestration of cellular contents into a double-membrane vesicle, the autophagosome. Although recent studies have demonstrated that autophagy supports cell migration, the underlying mechanisms remain unknown. Using live-cell imaging, we uncover that autophagy promotes optimal migratory rate and facilitates the dynamic assembly and disassembly of cell-matrix focal adhesions (FAs), which is essential for efficient motility. Additionally, our studies reveal that autophagosomes associate with FAs primarily during disassembly, suggesting autophagy locally facilitates the destabilization of cell-matrix contact sites. Furthermore, we identify the selective autophagy cargo receptor neighbor of BRCA1 (NBR1) as a key mediator of autophagy-dependent FA remodeling. NBR 1 depletion impairs FA turnover and decreases targeting of autophagosomes to FAs, whereas ectopic expression of autophagy-competent, but not autophagy-defective, NBR1 enhances FA disassembly and reduces FA lifetime during migration. Our findings provide mechanistic insight into how autophagy promotes migration by revealing a requirement for NBR1-mediated selective autophagy in enabling FA disassembly in motile cells.

Introduction

Cell migration is essential for tissue morphogenesis during development, immune function, and wound healing and is deregulated during pathological processes such as cancer (Ridley et al., 2003; Friedl and Wolf, 2010). Migration is a highly integrated process involving tight spatiotemporal control of signaling and structural networks throughout the cell. Chief among these are integrin-based focal adhesions (FAs) through which cells engage in adhesive contacts with the surrounding ECM . In addition to integrins, FAs are comprised of signaling and adapter proteins that serve as large, macromolecular biochemical and physical scaffolds linking the ECM to the intracellular actin cytoskeleton (Gardel et al., 2010; Geiger and Yamada, 2011). As such, FAs direct migration in part by mechanically generating forces for movement. Specifically, rapid cycles of FA assembly and disassembly, or turnover, at the leading edge of migrating cells are necessary for productive migration. FA assembly allows cells to establish traction for forward movement, whereas subsequent disassembly of FAs enables efficient displacement of the advancing cell (Gardel et al., 2010; Geiger and Yamada, 2011; Wolfenson et al., 2013).

Given the prominent role of cell migration in many physiological and pathological processes, understanding the regulation of FA dynamics is a topic of intense study. It is well established that FA assembly involves hierarchical recruitment of FA proteins because of phosphorylation and tension-induced conformational changes that progressively enable protein–protein interactions, but it is not completely certain how these events are regulated (Wolfenson et al., 2013). Although FA disassembly has also been shown to require phosphorylation of FA proteins (Webb et al., 2004) and recent work demonstrates that microtubule-induced FA disassembly involves extracellular proteolysis (Stehbens et al., 2014), how FA disassembly is spatiotemporally coordinated at the leading edge of migrating cells remains unclear.

Autophagy is an evolutionarily conserved process of cellular self-degradation that involves formation of a double-membrane vesicle, the autophagosome, which sequesters cytoplasmic material for delivery to lysosomes (Feng et al., 2014). Although traditionally viewed as a vital pathway supporting cellular homeostasis and adaptation to stress, autophagy is implicated in a growing list of cellular functions (Murrow and Debnath, 2013). Recent studies demonstrate that autophagy inhibition impacts cell migration (Galavotti et al., 2013; Tuloup-Minguez et al., 2013; Lock et al., 2014; Zhan et al., 2014). However, apart from establishing a genetic requirement for essential autophagy

Correspondence to Jayanta Debnath: Jayanta.Debnath@ucsf.edu

Abbreviations used in this paper: ATG, autophagy regulator; FA, focal adhesion; iBMK, immortalized baby mouse kidney; LC3, microtubule-associated protein 1 light chain 3; LIR, LC3-interacting region; NBR1, neighbor of BRCA1; NDP52, nuclear dot protein 52; OPTN, optineurin; p62, p62/sequestosome 1; PyMT, polyoma middle T; SIM, structured illumination microscopy; TIRF, total internal reflection fluorescence; UBA, ubiquitin-binding domain.

The Rockefeller University Press $30.00
J. Cell Biol. Vol. 212 No. 5 577–590
www.jcb.org/cgi/doi/10.1083/jcb.201503075

regulators (ATGs) in mediating these phenotypes, the mechanistic basis of autophagy-dependent motility is not known.

Therefore, we sought to establish how the autophagy pathway regulates motility and demonstrate here that autophagy facilitates leading edge FA turnover during migration. ATG depletion diminishes migratory rate and stabilizes FAs, as evidenced morphologically by enlarged leading edge FAs and dynamically by longer-lived FAs that exhibit reduced rates of FA assembly and disassembly. We also show that autophagosomes localize to dynamic leading edge FAs; temporally, this association occurs principally during FA disassembly. Finally, our studies uncover an important role for the selective autophagy cargo receptor neighbor of BRCA1 (NBR1) in enabling both cell motility and autophagy-dependent FA turnover. Because autophagy cargo receptors mediate sequestration of substrates into autophagosomes, we propose a model in which NBR1 facilitates autophagic targeting of FAs, thereby driving FA turnover to optimize migration.

Results

Autophagy-deficient cells have reduced migration rates and increased FA size

We previously demonstrated that autophagy supports the migration of $HRas^{V12}$-transformed MCF10A (MCF10A-Ras) cells and the mutant KRas-transformed human breast cancer cell line MDA-MB-231 (Lock et al., 2014). To extend these findings, we evaluated the role of autophagy during migration of additional epithelial cells in which autophagy was inhibited via genetic loss of function of multiple ATGs essential for autophagosome formation. Stable knockdown of ATG7 or ATG12 in wild-type MCF10A mammary epithelial cells or polyoma middle T (PyMT) mouse mammary tumor cells impaired autophagy, as indicated by the reduced lysosomal turnover of lipidated microtubule-associated protein 1 light chain 3 (LC3-II), a biochemical marker of autophagic flux (Fig. S1, A and B). Similarly, autophagy was eliminated in immortalized baby mouse kidney (iBMK) cells derived from *Atg5*$^{-/-}$ mice (Fig. S1 C). Consistent with previous results, autophagy inhibition caused by ATG depletion impaired the motility of both MCF 10A cells and PyMT cells during in vitro scratch-wound closure assays (Fig. S1, D–G). Likewise, *Atg5*$^{-/-}$ iBMK cells exhibited reduced migration compared with *Atg5*$^{+/+}$ cells (Fig. S1, H and I). These data corroborate that autophagy promotes the motility of multiple cell types.

Next, we used MCF10A-Ras cells to more precisely dissect how autophagy regulates migration. Using live-cell imaging to track individual migrating cells over 3 h during wound closure, we found that autophagy-deficient cells, caused by stable ATG7 or ATG12 depletion, failed to move as far as control cells, resulting in an ∼40% reduction in migration speed upon ATG depletion (Fig. 1, A–C; Fig. S1 A; and Video 1). Because FAs generate force for movement and anchor cells to their substratum, they are established as critical determinants of migration rate in diverse cell types (DiMilla et al., 1991, 1993; Huttenlocher et al., 1996; Palecek et al., 1997; Gupton and Waterman-Storer, 2006; Friedl and Wolf, 2010). Therefore, we analyzed FAs at the leading edge of wound edge cells by immunofluorescence for endogenous paxillin, a marker of FAs, to determine if cell-ECM adhesion is affected by autophagy deficiency. Measurements of FA area showed that ATG depletion resulted in significantly increased FA size, indicating that FAs may be stabilized in autophagy-deficient cells (Fig. 1, D and E). In contrast, F-actin (phalloidin) staining did not show obvious differences in the actin cytoskeleton (Fig. 1 D). We similarly observed that FAs in autophagy-inhibited PyMT cells were larger than FAs in control cells (Fig. S1 J). Because optimal migration rate is achieved at intermediate levels of integrin-mediated adhesion strength (DiMilla et al., 1991, 1993; Huttenlocher et al., 1996; Palecek et al., 1997; Gupton and Waterman-Storer, 2006), these data broached the possibility that enhanced cell-ECM adhesion resulting from FA stabilization upon autophagy inhibition contributes to reduced migration by impeding productive movement.

Autophagy inhibition impairs FA turnover

Because FAs are highly dynamic during migration, the FA defects observed upon autophagy inhibition may result from perturbations in FA assembly or disassembly. To establish if autophagy impacts specific aspects of FA turnover, we generated control and ATG knockdown cells expressing paxillin-mCherry, an established reporter of dynamic FAs, and used live-cell spinning disk confocal microscopy to scrutinize leading edge FAs during migration (Stehbens et al., 2014; Stehbens and Wittmann, 2014). Similar to endogenous paxillin immunostaining (Fig. 1, D and E), paxillin-mCherry–labeled FAs appeared larger in autophagy-inhibited cells, and fewer cycles of FA assembly and disassembly were apparent at the leading edge of ATG-depleted cells in comparison to autophagy-competent controls (Fig. 2 A and Videos 2 and 3). To rigorously quantify differences in FA dynamics, we used established methods in which fluorescence intensity profiles of paxillin-mCherry over time were fitted with a logistic function and a single exponential decay function to determine rate constants for assembly and disassembly, respectively; FA lifetime was calculated as the amount of time paxillin-mCherry fluorescence intensity remained above half its maximal value (Fig. 2 B; Webb et al., 2004; Meenderink et al., 2010; Stehbens et al., 2014; Stehbens and Wittmann, 2014). This analysis showed that in comparison to controls, the rate of assembly was reduced by 30% and 37% for ATG7 and ATG12 knockdown, respectively, and disassembly rates decreased by 48% and 42% upon ATG7 and ATG12 depletion, respectively (Fig. 2 C). Overall, these changes led to stabilization of FAs in autophagy-deficient cells in which lifetimes were significantly increased by 86% with ATG7 depletion and 68% with ATG12 depletion (Fig. 2 C). These results substantiate that autophagy is required for efficient leading edge FA turnover in migrating cells.

Autophagy-deficient cells exhibit enhanced cell spreading

In addition to affecting motility, increased stabilization of FAs is also associated with enhanced cell spreading (Cavalcanti-Adam et al., 2007; Friedl and Wolf, 2010). Accordingly, we performed cell spreading assays to further assess the functional impact of FA stabilization upon autophagy inhibition. We generated control and ATG knockdown cells expressing ZsGreen for tracking purposes, and using live-cell imaging, we monitored the spreading of cells upon replating over 3 h. These assays revealed that autophagy-deficient cells underwent prolonged spreading, resulting in increased cell area compared with controls (Fig. 3 A). Quantification of the area of ZsGreen-expressing cells fixed at 1 h after replating further confirmed that ATG-depleted cells

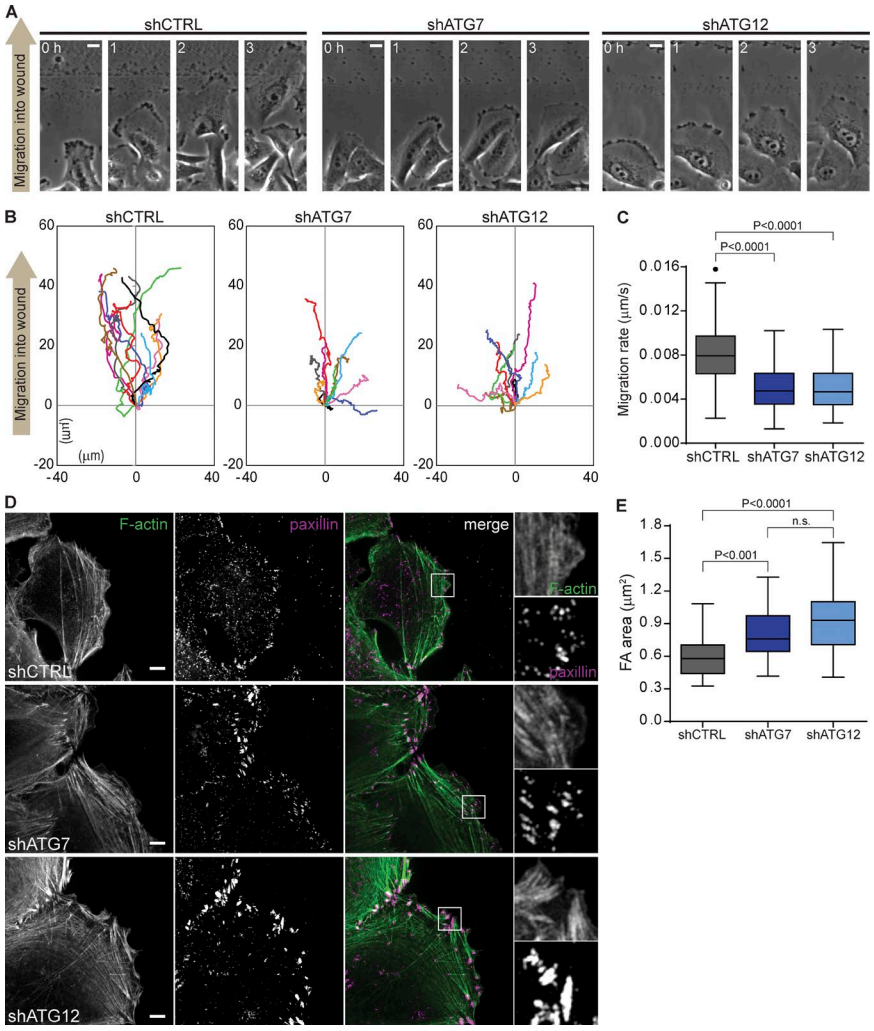

Figure 1. **Impaired migration rate and increased FA size in autophagy-deficient cells.** (A) Representative phase-contrast microscopy time-lapse sequences of single cells expressing shControl (CTRL; left), shATG7 (middle), or shATG12 (right) tracked over 3 h after wounding. Elapsed time (h) in top left of images. Bars, 10 µm. These images correspond to Video 1. (B) Migration paths of individual shCTRL (left), shATG7 (middle), or shATG12 (right) cells showing total distance traveled over 3 h. Cell position over time was used to generate paths and was determined by manually tracking cell nucleoli in each frame over the course of the time lapse. n = 10 representative cells shown per condition, and each colored track represents an independent cell. The starting position for each cell was normalized to 0 µm, 0 µm on the x, y axes. (C) Quantification of migration rate of individual tracked cells determined as total distance traveled divided by the total time of migration ($d/t_f - t_0$). Data presented as median (line), first and third quartile (box), and whiskers extend to ±1.5 times the interquartile range. Individual data points outside of this range are shown. n = 155 cells for shCTRL, n = 121 cells for shATG7, and n = 115 cells for shATG12, pooled from three independent experiments.P-values calculated using a nonparametric Kruskall-Wallis test followed by Dunn post-hoc test. (D) Representative immunofluorescence images of migrating wound edge cells expressing shCTRL (top), shATG7 (middle), or shATG12 (bottom) stained for endogenous F-actin (green) and paxillin (magenta) to mark FAs. Right panels show enlarged insets of boxed region in merged images. Bars, 5 µm. Insets are magnified 3.7-fold. (E) Quantification of the area of leading edge FAs in migrating wound edge cells determined by manually outlining anti-paxillin-labeled FAs. Data presented as median (line), first and third quartile (box), and whiskers extend to ±1.5 times the interquartile range. n = 713 FAs for shCTRL, n = 511 FAs for shATG7, and n = 430 FAs for shATG12, pooled from two independent experiments. P-values calculated using a nonparametric Kruskall-Wallis test followed by Dunn post-hoc test. n.s., not significant.

exhibited a significant increase in cell area compared with autophagy-competent cells (Fig. 3, B and C). Together with our quantitative analysis of FAs in migrating cells, these findings point to a broader role for autophagy in modulating adhesion-dependent phenotypes.

Autophagosomes localize to FAs during disassembly in migrating cells

Typically, autophagy functions through the local and direct sequestration of cellular material into the forming autophagosome, which eventually fuses with lysosomes for cargo degradation (Murrow and Debnath, 2013; Feng et al., 2014). Hence, we reasoned that autophagy-dependent FA turnover may entail the close local apposition of autophagosomes with dynamic FAs during migration. To test this prediction, we generated cells coexpressing paxillin-mCherry and GFP-LC3, which marks autophagosomes, and observed that autophagosomes localized throughout the leading edge of migrating cells (Fig. 4 A and Video 4). We enumerated adhesions targeted by GFP-LC3, defined as GFP-LC3 puncta in direct contact with paxillin-mCherry–labeled FAs and found that 40% of dynamic FAs were directly targeted by autophagosomes and that autophagosomes were enriched by 40-fold at FAs compared with non-FA areas at the leading edge (Fig. 4, B–F; and Videos 5 and 6). Of note, these experiments may underestimate the actual number of targeted FAs because of the rapid intracellular dynamics of GFP-LC3–labeled vesicles. In addition, we used structured illumination microscopy (SIM) and total internal reflection fluorescence (TIRF) microscopy to better observe the spatial relationship between autophagosomes and FAs. SIM, which provides improved resolution over confocal imaging, corroborated that autophagosomes localize to leading edge FAs (Fig. S2 A). Likewise, TIRF imaging further verified that autophagosomes are localized to leading edge FAs at the basal surface of migrating cells (Fig. S2 B). Furthermore, during cell spreading, we similarly observed GFP-LC3 puncta to be associated with dynamic FAs throughout the periphery of the cell, further confirming that autophagosomes are locally targeted to FAs (Fig. S2 C).

We next determined if autophagosome targeting to FAs proceeds in a temporally specific manner. Interestingly, a limited number of targeting events occurred during FA assembly or when FAs were relatively stable; rather, most GFP-LC3 targeting events occurred during FA disassembly (Fig. 4, E–G; and Video 6). Together with our data showing that autophagy is functionally required for FA turnover, these results support

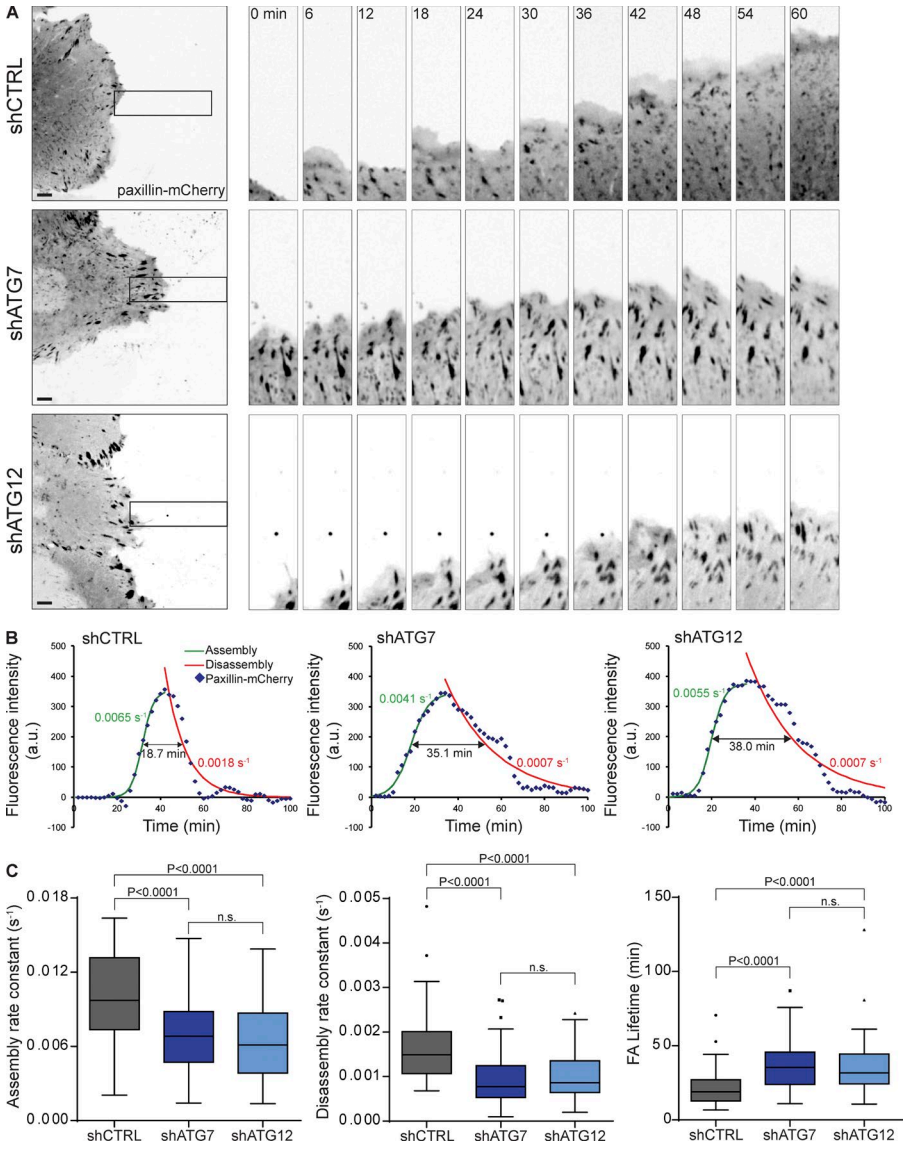

Figure 2. **Autophagy promotes FA turnover in migrating cells.** (A) Spinning disk confocal microscopy time-lapse sequences of migrating cells expressing paxillin-mCherry (black) to monitor FA dynamics. Left panels show representative cells expressing shCTRL (top), shATG7 (middle), or shATG12 (bottom). Image sequences of boxed regions have been rotated such that the cell edge with dynamic FAs is moving upward vertically. Elapsed time (min) shown in top left. Bars, 5 µm. Insets are magnified twofold. These images correspond to Videos 2 and 3. (B) Example plots of paxillin-mCherry fluorescence intensity (y axis) over time (x axis) for shCTRL (left), shATG7 (middle), and shATG12 (right) cells used for calculating FA turnover parameters in C. Plots generated by manually tracking individual FAs over time, and each data point is a three-frame running mean of intensity value. The green line represents FA assembly fitted with a logistic function, and the red line represents FA disassembly fitted with an exponential decay function. The lifetime is the time spent above half-maximum fluorescence intensity (double arrow). The values of each parameter are indicated for the specific curves shown (assembly rate constant in green, disassembly rate constant in red, and lifetime in black). (C) Quantification of assembly rate constants (left), disassembly rate constants (middle), and lifetime (right) for FAs in cells expressing shCTRL, shATG7, or shATG12. Data presented as median (line), first and third quartile (box), and whiskers extend to ±1.5 times the interquartile range. Individual data points outside of this range are shown. n = 64 FAs for shCTRL, n = 62 FAs for shATG7, and n = 51 FAs for shATG12, pooled from four independent experiments. P-values calculated using a nonparametric Kruskall-Wallis test followed by Dunn post-hoc test. n.s., not significant.

that autophagy impacts leading edge FAs by proximally facilitating disassembly. This autophagy-dependent FA remodeling may involve the local sequestration of FA components into autophagosomes to promote FA destabilization and disassembly. In support, multiple FA proteins, including paxillin, vinculin, and zyxin, were present in GFP-LC3–labeled autophagosomes of migrating cells (Fig. S2 D).

The selective autophagy cargo receptor NBR1 promotes cell migration and FA turnover

Given the highly specific targeting of autophagosomes to FAs during disassembly, and because FA turnover is exquisitely coordinated to optimize migration and adhesion (Gardel et al., 2010; Geiger and Yamada, 2011; Wolfenson et al., 2013), we hypothesized that a tightly controlled mechanism would be necessary to direct autophagic targeting of FAs. Notably, FAs are large protein complexes (Geiger and Zaidel-Bar, 2012), and autophagy has been shown to target large intracellular macromolecular assemblies, such as iron-containing ferritin complexes (Dowdle et al., 2014; Mancias et al., 2014) and midbody derivatives during the final stages of cytokinesis (Pohl and Jentsch, 2009; Kuo et al., 2011). The autophagic targeting of these structures is mediated by autophagy cargo receptors, which promote the selective degradation of cellular substrates (Johansen and Lamark, 2011; Rogov et al., 2014). These molecules bind cargo marked with degradation signals, most commonly ubiquitin, through their ubiquitin-binding domains (UBAs; Kraft et al., 2010) and typically possess an LC3-interacting region (LIR) motif, which allows them to bind to LC3 and other ATG8 isoforms present on developing autophagosomes (Birgisdottir et al., 2013). Because of these unique characteristics, we sought to determine if autophagy cargo receptors support migration and FA dynamics.

To initially establish if individual autophagy cargo receptors regulate migration, we performed scratch-wound closure assays with cells transiently depleted for several of the major known receptors, including p62/sequestosome 1 (p62), NBR1, optineurin (OPTN), and nuclear dot protein 52 (NDP52). We identified NBR1 as the only cargo receptor whose knockdown significantly attenuated wound closure (Fig. 5, A and B; and Fig. S3 A). To verify this result, we generated stable pools of cells with shRNA against NBR1 (Fig. S3 B). In agreement with our findings using transient, siRNA-mediated depletion, stable NBR1 knockdown also significantly inhibited migration (Fig. 5,

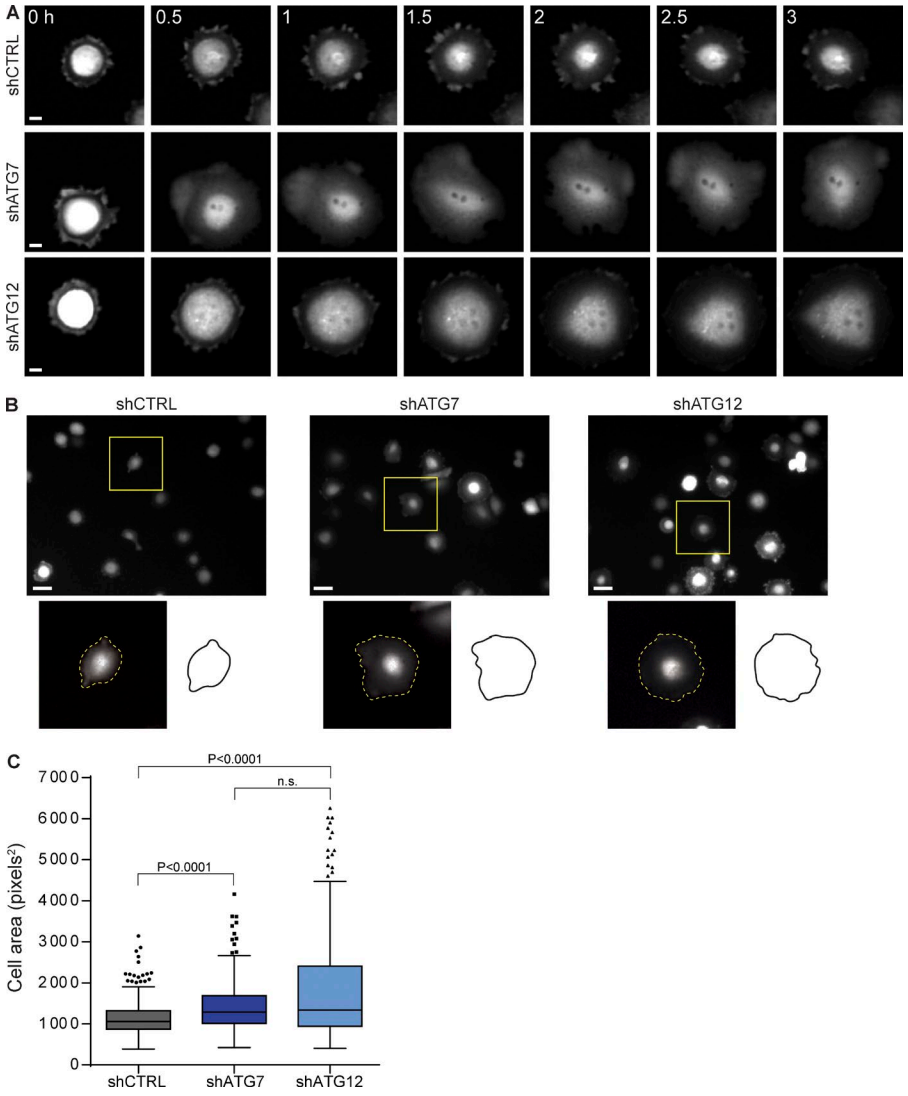

Figure 3. **Autophagy inhibition results in enhanced cell spreading.** (A) Spinning disk confocal microscopy time-lapse sequences of cells expressing ZsGreen during spreading after replating. Representative shCTRL (top), shATG 7 (middle), or shATG12 (bottom) cells shown over a 3-h time course. Elapsed time (h) indicated in top left of images. Bars, 10 µm. (B) Representative images of ZsGreen-expressing cells fixed 1 h after replating used for quantification of cell area in C. Whole field images shown with enlarged boxed insets of individual cells at bottom left. Tracing of individual cell in inset shown at bottom right. Bars, 50 µm. Insets are magnified 2.4-fold. (C) Quantification of area of cells fixed 1 h after replating. Area determined by manually outlining individual ZsGreen-expressing cell borders. Data presented as median (line), first and third quartile (box), and whiskers extend to ±1.5 times the interquartile range. Individual data points outside of this range are shown. n = 315 cells for shCTRL, n = 351 cells for shATG7, and n = 306 cells for shATG12, pooled from three independent experiments. P-values were calculated using a nonparametric Kruskall-Wallis test followed by Dunn post-hoc test. n.s., not significant.

C and D). Importantly, in contrast with ATG knockdown, NBR 1 depletion did not affect basal autophagy levels (Fig. S3 C).

To further dissect the role of NBR1 in motility, we measured FA dynamics in paxillin-mCherry–expressing cells after stable NBR1 knockdown. Similar to ATG depletion, NBR1 loss of function decreased the rates of FA assembly and disassembly by 32% and 41%, respectively, leading to an overall 81% increase in FA lifetime compared with controls (Fig. 5, E and F; and Videos 7 and 8). Consistent with this role for NBR1 in facilitating FA turnover, endogenous NBR1 colocalized with anti-paxillin–labeled FAs, and GFP-NBR1 associated with and was significantly enriched at leading edge FAs in live migrating cells (Fig. S3, D–F; and Video 9). Furthermore, NBR 1-depleted ZsGreen-expressing cells underwent prolonged spreading compared with control cells and exhibited increased cell area at 1 h after replating (Fig. S4, A–C). Collectively, these results demonstrate that NBR1 loss of function phenocopies the effects of autophagy inhibition on both FA turnover and adhesion-dependent processes, indicating NBR1 and autophagy may coordinately facilitate FA remodeling through a common pathway of NBR1-mediated selective autophagy. Moreover, we uncover that NBR1, like autophagosomes, localizes to FAs, further supporting that NBR1-mediated selective autophagy proximally impacts FA remodeling.

NBR1-dependent selective autophagy promotes FA disassembly

Because NBR1 is a multidomain scaffold protein that may serve both autophagy-dependent and -independent functions, we next sought to more precisely ascertain if NBR1-mediated FA turnover is associated with its role in selective autophagy. NBR1-dependent selective autophagy requires that it locally promote targeting of autophagosomes to substrates destined for autophagic turnover; therefore, we hypothesized that NBR 1 would colocalize with a high proportion of FA-associated autophagosomes. Indeed, in migrating cells stably expressing paxillin-mTurquoise, Venus-LC3, and mCherry-NBR1, NBR1 was localized to 80% of FA-associated autophagosomes (Fig. 6, A and B). Most importantly, we uncovered that NBR1 depletion significantly attenuated the targeting of autophagosomes to dynamic, leading edge FAs (Fig. 6 C), thereby confirming the functional requirement of NBR1 in locally facilitating autophagic targeting of FAs. Collectively, these data provide evidence for a localized pathway of NBR1-mediated autophagic targeting of FAs.

Autophagy cargo recognition by NBR1 requires that it interact with both potential substrates and forming autophagosomes. Accordingly, we first assessed whether NBR1 interacts with FA components in cells ectopically expressing low levels

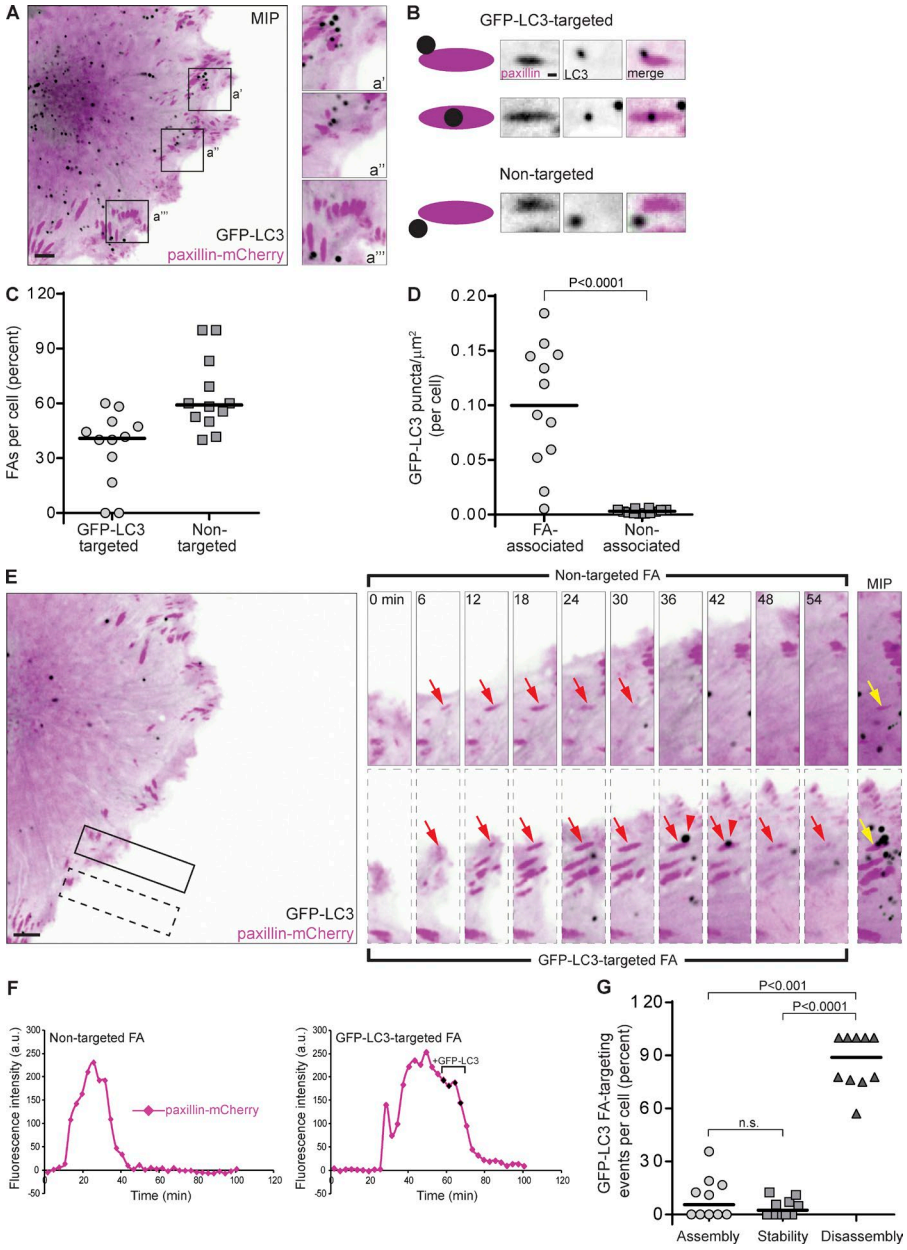

Figure 4. **Autophagosomes associate with dynamic FAs during disassembly.** (A) Spinning disk confocal microscopy of a migrating cell expressing GFP-LC3 (black) to label autophagosomes and paxillin-mCherry (magenta) to label FAs. Left panel shows maximum intensity projection (MIP) of a cell over 21 min, illustrating multiple associations between autophagosomes and FAs. Boxed inset areas are enlarged in right panel. Bar, 5 µm. Insets are magnified twofold. (B) Criteria for distinguishing GFP-LC3–targeted FAs versus nontargeted FAs. Left illustration depicts representations of targeted FAs (top and middle) and nontargeted FAs (bottom). Right images are examples of targeted and nontargeted FAs. Bar, 0.5 µm. (C) Quantification of the percentage of dynamic leading edge FAs per cell targeted by autophagosomes. FAs were randomly chosen independent of the GFP channel and then manually tracked from their appearance to disappearance for evidence of direct contact by GFP-LC3 vesicles. Scatter plot shows individual single cells (n = 12 total cells) and median (line), representing 129 total FAs analyzed from two independent experiments. (D) Analysis of GFP-LC3 vesicles in FA areas and non-FA areas at the leading edge of migrating cells. The total number of vesicles at FAs or in non-FA areas was counted and normalized to the total area for FA or non-FA regions, respectively. Scatter plot shows individual single cells (n = 12 total cells) and mean (line), representing 196 total leading edge GFP-LC3 vesicles analyzed from two independent experiments. P-value determined using unpaired t test. (E) Spinning disk confocal microscopy time-lapse sequences of representative targeted (box with dotted border, bottom) and nontargeted (box with solid border, top) FAs. Insets rotated such that leading edge is moving upward vertically. Arrows track single FAs over time, with autophagosome targeting indicated by arrowheads. Elapsed time (min) shown in top left of images. Right-most panels show MIP for each FA (arrow) shown in the corresponding time-lapse sequence. Bar, 5 µm. Insets are magnified 1.5-fold. (F) Representative paxillin-mCherry fluorescence intensity (y axis) plots over time (x axis) for the FAs shown in E. Frames in which GFP-LC3 was in direct contact with FAs are indicated by black data points and bracketing (right plot). (G) Temporal analysis of GFP-LC3 targeting to FAs. The phase during which GFP-LC3 associated with FAs was determined by counting the total number of GFP-LC3 targeting events in C and determining when during FA turnover each event occurred; if FAs were targeted multiple times during their lifetime, each event was independently counted. Scatter plot shows individual cells (n = 12 total cells) and median (line), representing 114 total targeting events analyzed from two independent experiments. P-values were calculated using a nonparametric Kruskall-Wallis test followed by Dunn post-hoc test. n.s., not significant. Images in this figure correspond to Videos 4–6.

of GFP-NBR1. GFP-NBR1 interacted with multiple endogenous FA proteins, including paxillin, vinculin, zyxin, and FAK, indicating that such biochemical interactions may enable localization of NBR1 to FAs (Fig. S5 A). As a positive control, we confirmed the previously established interaction of GFP-NBR1 with p62 in these cells (Lange et al., 2005; Kirkin et al., 2009; Fig. S5 A). Next, we used a gain-of-function approach to scrutinize the requirement of NBR1 interaction with LC3 in autophagy-dependent FA turnover. We generated cells overexpressing wild-type GFP-NBR1 or a mutant NBR1 lacking the LIR motif (GFP-NBR1 ΔLIR) required for binding to LC3/ATG8, thereby rendering it autophagy-incompetent (Kirkin et al., 2009; Waters et al., 2009; Fig. 6 D). In contrast to wild-type GFP-NBR1, GFP-NBR1 ΔLIR was resistant to nutrient starvation-induced autophagic degradation, confirming this mutant to be autophagy-incompetent (Fig. 6 E). GFP-NBR1 was ectopically expressed in paxillin-mCherry cells to test if increased NBR1 was sufficient to enhance FA turnover. Compared with GFP alone, expression of GFP-NBR1 significantly increased FA turnover. Although GFP-NBR1 did not impact FA assembly, it significantly enhanced FA disassembly by 46%, leading to an overall 29% decrease in FA lifetime (Figs. 6 F and S5 B). In contrast, GFP-NBR1 ΔLIR did not significantly affect FA assembly, disassembly, or lifetime (Figs. 6 F and S5 B). Therefore, the interaction of NBR1 with LC3, and hence the ability of this cargo receptor to facilitate selective autophagy, is absolutely essential

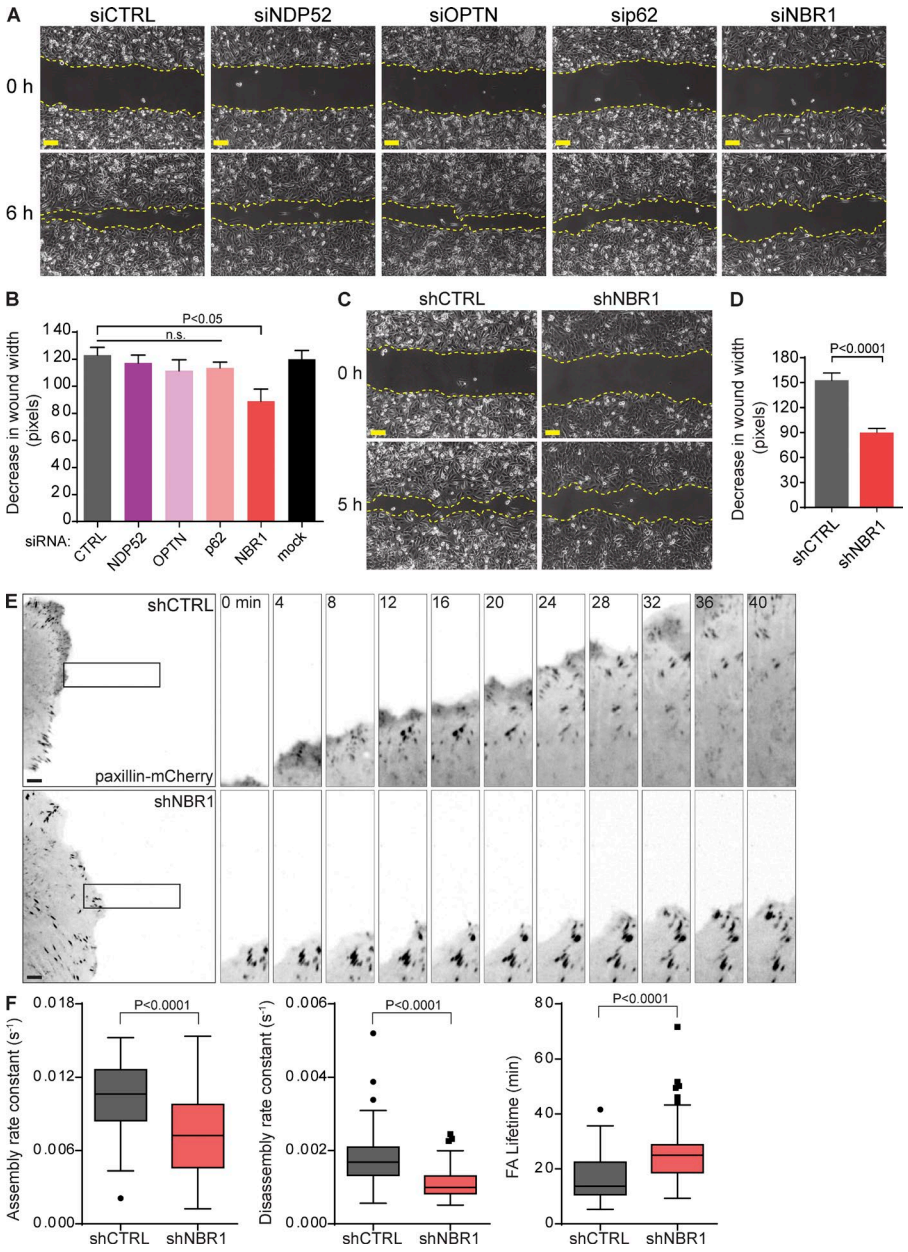

Figure 5. **NBR1 facilitates cell migration and FA turnover.** (A) Representative phase-contrast microscopy images at time of wounding (0 h) and 6 h after wounding for cells expressing control siRNA (CTRL) or siRNA against NDP 52, OPTN, p62, or NBR1. Dashed yellow lines highlight wound boundaries. Bars, 100 µm. (B) Quantification of wound closure over 6 h by cells expressing indicated siRNAs. The decrease in wound width was determined by subtracting the final width at 6 h from the initial width at 0 h. Bar graph shows mean + SEM , representing $n = 8$ wounds for siCTRL, $n = 8$ wounds for siNDP52, $n = 8$ wounds for siOPTN, $n = 6$ wounds for sip62, $n = 6$ wounds for siNBR1, and $n = 5$ wounds for mock (no siRNA) pooled from four independent experiments. P-values calculated using one-way analysis of variance followed by Tukey post-hoc test. n.s., not significant. (C) Representative phase-contrast microscopy images of cells expressing shCTRL or shNBR1 at time of wounding (0 h) and at 5 h after wounding. Dashed yellow lines highlight wound boundaries. Bars, 100 µm. (D) Quantification of wound closure over 5 h by shCTRL and shNBR1 cells. Bar graph shows mean + SEM, representing $n = 12$ wounds for shCTRL and $n = 15$ wounds for shNBR1 pooled from three independent experiments. P-value determined using unpaired *t* test. (E) Spinning disk confocal microscopy time-lapse sequences of cells expressing paxillin-mCherry (black) to monitor FA dynamics. Left panels show representative cells expressing shCTRL (top) or shNBR1 (bottom). Image sequences of boxed regions on the right have been rotated such that the cell edge with dynamic FAs is moving upward vertically. Elapsed time (min) in top left of images. Bars, 5 µm. Insets are magnified twofold. These images correspond to Videos 7 and 8. (F) Quantification of FA assembly rate constants (left), disassembly rate constants (middle), and lifetime (right) for FAs in shCTRL or shNBR1 cells. Data presented as median (line), first and third quartile (box), and whiskers extend to ±1.5 times the interquartile range. Individual data points outside of this range are shown. $n = 53$ FAs for shCTRL and $n = 58$ FAs for shNBR1, pooled from three independent experiments. P-value calculated using a nonparametric Mann-Whitney test.

for its role in enabling FA turnover. Finally, because autophagy cargo recognition by NBR1 also involves the binding of ubiquitinated substrates via its UBA, we tested the effects of a mutant NBR1 lacking this UBA (GFP-NBR1 ΔUBA) on FA dynamics. Similar to GFP-NBR1 ΔLIR, GFP-NBR1 ΔUBA did not significantly impact FA disassembly or turnover (Figs. 6 F and S5 B). Overall, these results delineate a specific role for NBR1-mediated selective autophagy in regulating FA turnover by promoting FA disassembly in migrating cells.

Discussion

In summary, we present evidence for autophagy as a mechanism for FA turnover at the leading edge of migrating cells and implicate the selective autophagy cargo receptor, NBR1, as a key mediator of this process. Using live-cell imaging to directly visualize FAs, we uncover that autophagy supports FA turnover and that autophagosomes target FAs during disassembly. Overall, these data suggest a role for autophagy in facilitating FA turnover by locally promoting FA disassembly. Although autophagosomes are found preferentially associated with disassembling FAs, it is important to note that ATG knockdown functionally impairs both FA assembly and disassembly. Therefore, although disassembly may be proximally modulated by autophagy, we cannot rule out that autophagy regulates FA assembly by more indirect mechanisms that do not necessarily involve the localization of autophagosomes to FAs.

There is evidence that autophagy directs the endocytic recycling of β1-integrins. However, the activation of this pathway is only observed during extreme nutrient deprivation conditions in which cells are incubated in HBSS to induce autophagy. As a result, it remains uncertain whether the autophagy pathway alters integrin recycling to impact migration in broader contexts (Tuloup-Minguez et al., 2013). Although autophagy may impact cell motility via multiple mechanisms, our results

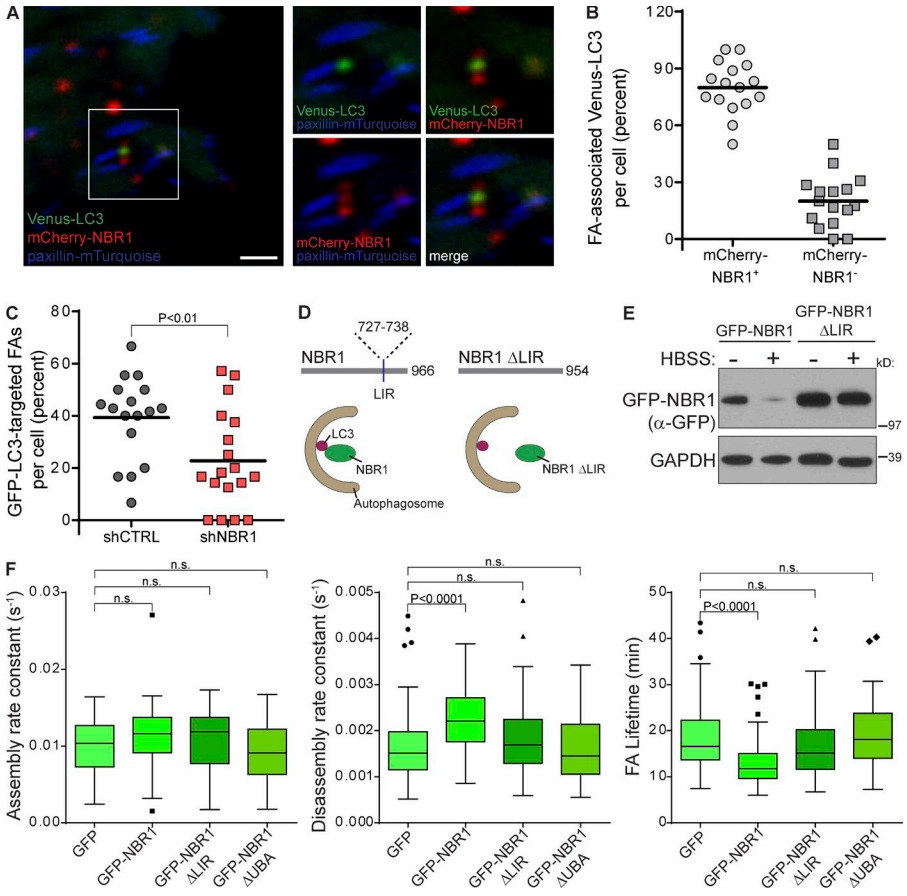

Figure 6. **NBR1-mediated selective autophagy promotes FA disassembly.** (A) Representative spinning disk confocal image of a migrating cell stably expressing paxillin-mTurquoise, Venus-LC3, and mCherry-NBR1. Whole-cell merged image shown at left and enlarged boxed insets of two- and three-color merged images shown at right. Bar, 2.5 µm. Insets are magnified 1.4-fold. (B) Quantification of mCherry-NBR1 colocalization with FA-associated Venus-LC3 vesicles. FA-associated Venus-LC3 vesicles were identified as described in Fig. 4 B, and then the number of mCherry-NBR1-positive and -negative vesicles were enumerated. Scatter plot shows individual single cells (n = 16 total cells) and mean (line), representing 170 total FA-associated Venus-LC3 vesicles analyzed from two independent experiments. (C) Quantification of the percentage of dynamic leading edge FAs per cell targeted by autophagosomes in shCTRL or shNBR1 cells. FAs were randomly chosen independent of the GFP channel and then manually tracked for evidence of direct contact by GFP-LC3 vesicles as described in Fig. 4 B. Scatter plot shows individual single cells (n = 17 cells for shCTRL and n = 18 cells for shNBR1) and mean (line), representing 165 FAs for shCTRL and 159 FAs for shNBR1 analyzed from two independent experiments. P-value determined using unpaired t test. (D) Schematic of wild-type NBR1 (left) and autophagy-defective NBR 1 (NBR1 ΔLIR, right) resulting from deletion of the LIR (aa 727–738, depicted as vertical line). Bottom diagram demonstrates inability of NBR1 ΔLIR to bind LC3 (right) and be recruited into autophagosomes, unlike wild-type NBR 1 (left). (E) Nutrient-starved (HBSS, 4 h) HEK-293T cells ectopically expressing wild-type GFP-NBR1 or GFP-NBR1 ΔLIR. GAPDH is loading control. (F) Quantification of FA assembly rate constants (left), disassembly rate constants (middle), and lifetime (right) for FAs in cells expressing GFP control, GFP-NBR1, GFP-NBR1 ΔLIR, or GFP-NBR1 ΔUBA. Data presented as median (line), first and third quartile (box), and whiskers extend to ±1.5 times the interquartile range. Individual data points outside of this are shown. n = 99 FAs for GFP control, n = 84 FAs for GFP-NBR1, n = 62 FAs for GFP-NBR1 ΔLIR, and n = 62 FAs for GFP-NBR1 ΔUBA, pooled from four independent experiments. P-values calculated using a nonparametric Kruskall-Wallis test followed by Dunn post-hoc test. n.s., not significant.

here most clearly implicate autophagy in promoting leading edge FA turnover, which functions as a crucial and distinct contributor to migration.

Significantly, our results expand on the growing importance of selective autophagy receptors, namely NBR1, in controlling essential cellular functions. Our findings that loss of NBR1 function inhibits migration and leading edge FA turnover, that NBR1 is required for efficient targeting of autophagosomes to FAs, that only autophagy-competent NBR1 is sufficient to specifically drive FA disassembly, and that NBR1 colocalizes with autophagosomes at dynamic FAs all support that cargo receptor–mediated autophagy fine-tunes migratory capacity by optimizing adhesion site turnover. Like other autophagy cargo receptors, NBR1 enables the selective capture of cellular substrates into autophagosomes. Therefore, our work broaches the hypothesis that NBR1 interacts with FA-associated proteins and recruits autophagosomes to FAs via binding of NBR1 to LC3. This recruitment triggers autophagic sequestration or consumption of FA components, which facilitates FA disassembly. In support, we demonstrate that NBR1 biochemically interacts with multiple FA proteins and that FA components are localized to autophagosomes in migrating cells. Indeed, selective autophagy is an attractive candidate for mediating turnover of large macromolecular complexes, such as FAs, because it is the major homeostatic pathway through which bulky cellular cargo, such as organelles and protein aggregates, are sequestered and degraded (Murrow and Debnath, 2013).

During autophagy, cargo selection is often specified by ubiquitination of substrates (Kraft et al., 2010; Johansen and Lamark, 2011). E3 ubiquitin ligases constitute an integral arm of the adhesome, and FA proteins can be modified by ubiquitination (Schiller and Fässler, 2013; Wolfenson et al., 2013; Deng and Huang, 2014; Winograd-Katz et al., 2014). Despite being an important pathway for the turnover of ubiquitinated substrates, the role of autophagy in dictating the fate of FAs harboring ubiquitinated proteins has not been investigated. Our data demonstrate that the UBA of NBR1 is required for NBR 1-dependent FA disassembly, indicating a potentially important role for the recognition of ubiquitinated cargoes during autophagy-mediated FA turnover. In addition, ubiquitin-independent mechanisms of autophagy substrate selection also exist (Kraft et al., 2010), and FAs consist of hundreds of proteins (Geiger and Zaidel-Bar, 2012). Furthermore, NBR1 is a large multidomain scaffold (Whitehouse et al., 2002; Müller et al., 2006; Kirkin et al., 2009; Waters et al., 2009) with the ability to engage in many interactions. Given these potentially diverse mechanisms of cargo recognition, numerous interactions between NBR1 and FAs likely exist; accordingly, our biochemical studies indicate

that multiple FA proteins are able to interact with NBR1. Therefore, important topics for future study are to more comprehensively identify NBR1 binding partners at FAs and to elucidate how such interactions are regulated, both by ubiquitination and other pathways, to promote autophagosome recruitment to dynamic FAs during adhesion-dependent processes.

Finally, our results demonstrating that FA turnover is partially inhibited in autophagy-deficient cells reinforce that selective autophagic targeting of FAs only serves as one destabilizing mechanism to promote disassembly. Additional pathways, including phosphorylation mediated by FAK-Src signaling (Webb et al., 2004), endocytosis (Ezratty et al., 2005, 2009; Chao and Kunz, 2009), calpain cleavage (Franco et al., 2004; Chan et al., 2010; Cortesio et al., 2011), and ECM proteolysis (Shi and Sottile, 2011; Stehbens et al., 2014), have all been implicated in FA disassembly. Together with our current results demonstrating that autophagy supports FA turnover, these findings illustrate how cells engage diverse mechanisms to direct adhesion and migration. Going forward, a crucial unanswered question is how autophagy acts in concert with these other pathways to orchestrate FA remodeling.

Materials and methods

Cell culture

MCF10A and MCF10A-Ras mammary epithelial cells were cultured in DMEM/F12 supplemented with 5% horse serum, 20 ng/ml EGF, 0.5 µg/ml hydrocortisone, 100 ng/ml cholera toxin, 10 µg/ml insulin, penicillin, and streptomycin. PyMT mammary carcinoma cells (R221A clone; Martin et al., 2008; gift from B. Fingleton, Vanderbilt University, Nashville, TN) and HEK-293T cells were cultured in DMEM with 10% FBS, penicillin, and streptomycin. iBMK cells were a gift from E. White (Rutgers University, New Brunswick, NJ) and are now commercially available from Applied Biological Materials (T0082 and T3027). They were originally derived via stable transformation of primary kidney epithelial cells isolated from *Atg5*$^{+/+}$ and *Atg5*$^{-/-}$ isogenic newborn littermates (postnatal day 1, C57BL/6 genetic background) with adenovirus E1A and dominant negative p53 (p53DD; Mathew et al., 2008). They were cultured in DMEM with 10% FBS, penicillin, and streptomycin. For experiments, MCF10A-Ras cells were routinely incubated in assay media (DMEM/F12, 2% horse serum, 0.5 µg/ml hydrocortisone, 100 ng/ml cholera toxin, 10 µg/ml insulin, penicillin, and streptomycin; Debnath et al., 2003); 20 mM Hepes was added to the culture medium during live-cell imaging experiments.

cDNA constructs, retroviral and lentiviral vectors, and generation of stable cell lines

We previously generated pBabeneo-HRas^{V12}, pBabepuro-GFP-LC3 (22405; Addgene), pBabehygro-GFP-LC3, and pLenti6blast-paxillin-mCherry; our subcloning strategy for these plasmids has been described elsewhere (Hu et al., 2007; Fung et al., 2008; Lock et al., 2014; Stehbens et al., 2014). pMXs-IP-GFP-NBR1 and pMRX-IP-Venus-LC3 were gifts from N. Mizushima (University of Tokyo, Tokyo, Japan; 38283 and 58740; Addgene; Itakura and Mizushima, 2011; Koyama-Honda et al., 2013). pHIV-ZsGreen was provided by B. Welm (University of Utah School of Medicine, Salt Lake City, Utah; 18121; Addgene; Welm et al., 2008). pDest-mCherry-NBR1 was a gift from P. Kim (University of Toronto, Toronto, Ontario, Canada) and T. Johansen (University of Tromsø, Tromsø, Norway; Kirkin et al., 2009; Deosaran et al., 2013). Paxillin-mTurquoise, mCherry-vinculin, and zyxin-mCherry were from M. Davidson (Florida State University, Tallahassee, FL; 55573, 55159, and 55166; Addgene), and pLentiblast-GFP was provided by E. Campeau (University of Massachusetts Medical School, Worcester, MA; 19069; Addgene; Campeau et al., 2009). Lentiviral packaging and envelope plasmids pRSV-REV , pMD2Lg/pRRE, and pMD2.g were gifts from D. Trono (École Polytechnique Fédérale de Lausanne, Lausanne, Switzerland; 12253, 12251, and 12259; Addgene).

To generate pMXspuro-GFP, pMXspuro-GFP-NBR1, pMXspuro-GFP-NBR1 ΔLIR, and pMXspuro-GFP-NBR1 ΔUBA, GFP alone and GFP-NBR1 were first amplified from pMXs-IP-GFP-NBR 1 and subcloned into pcDNA3 (Life Technologies). Site-directed mutagenesis was then performed for deletion of aa 727–738 in NBR1 (NBR 1 ΔLIR) or to change aa 877 to a premature stop (NBR1 ΔUBA); GFP , GFP-NBR1, GFP-NBR1 ΔLIR, and GFP-NBR1 ΔUBA were subsequently subcloned into BamHI–XhoI sites of pMXspuro for retroviral expression (Kitamura et al., 2003). mCherry-NBR1 was PCR amplified from pDest-mCherry-NBR1 and subcloned into the BamHI–XhoI sites of pMXspuro to generate pMXspuro-mCherry-NBR1 for retroviral expression. To generate pLentiblast-paxillin-mTurquoise, paxillin-mTurquoise was PCR amplified and subcloned into the BamHI–SalI sites of pLentiblast-GFP for lentiviral expression.

Vesicular stomatitus virus G pseudotyped retroviruses were produced by transfection of a 293GPG retrovirus producer cell line (Ory et al., 1996) with 15 µg of expression cDNA using Lipofectamine 2000 (Life Technologies). Retroviral supernatants were collected at days 5–7 after transfection, filtered through a 0.45-µm filter, and stored at –80°C. Lentivirus was made using a four-plasmid, third-generation producer system (Dull et al., 1998) by cotransfecting HEK-293T cells with packaging and envelope vectors (2 µg of pRSV-REV, 2 µg of pMD2Lg/pRRE, and 4 µg of pMD2.g) and 12 µg of expression cDNA using Lipofectamine LTX/PLUS (Life Technologies). Lentiviral supernatants were collected 48 h after transfection, filtered through a 0.45-µm filter, and stored at –80°C. For infection with retroviruses and lentiviruses, 100,000 cells were seeded per well in six-well dishes the day before infection and incubated overnight with virus-containing supernatants supplemented with 8 µg/ml polybrene (Sigma-Aldrich). Stable cell lines were obtained by selecting with 200 µg/ml G418 (Sigma-Aldrich), 0.5–2 µg/ml puromycin (Sigma-Aldrich), 6 µg/ml blasticidin (Life Technologies), or 200 µg/ml hygromycin (Life Technologies). After stable pools were obtained, cells were cultured in the absence of selection agents.

RNA interference

For stable RNA interference, pLKO.1puro lentiviral plasmids with nontargeting shRNA or shRNA against ATG7 (human: NM_006395, mouse: NM_028835), human ATG12 (NM_004707), and human NBR 1 (NM_031858) were purchased from Sigma-Aldrich. The target sequence for shRNA against human ATG7 (TRCN0000007587) is 5′-CCCAGCTATTGGAACACTGTA-3′, against human ATG12 (TRC N0000007394) is 5′-TGGAACTCTCTATGAGTGTTT-3′, against mouse ATG7 (TRCN0000092163) is 5′-CCAGCTCTGAACTCAATA ATA-3′, and against human NBR1 (TRCN0000123161) is 5′-GCC AGGAACCAAGTTTATCAA-3′. The sequence of the nontargeting shRNA (SHC002; Sigma-Aldrich), which targets no known mammalian genes, is 5′-CAACAAGATGAAGAGCACCAA-3′. shRNA lentivirus was prepared as described above for lentiviral vectors. In brief, HEK-293T cells were cotransfected with packaging and envelope vectors and pLKO.1 shRNA expression plasmids. Virus was collected 48 h after transfection, filtered through a 0.45-µm filter, and stored at –80°C. Cells were seeded in six-well dishes and infected as described for generation of stable cell lines. Stable pools of knockdown cells were obtained by selecting with 2 µg/ml puromycin for 48 h. Cells were

used within one to two passages after selection for experiments. New stable pools were generated for each experimental repeat, and knockdown was verified by immunoblotting for each individual experiment.

For siRNA-mediated knockdown, ON-TARGETplus SMARTpool siRNAs were purchased from Dharmacon. The sense sequences of the individual duplexes comprising each pool are as follows: human p62/SQSTM1 (L-010230-00): 5′-GAACAGAUGGAGUCGGAUA-3′, 5′-GCAUUGAAGUUGAUAUCGA-3′, 5′-CCACAGGGCUGAAGGAAGC-3′, and 5′-GGACCCAUCUGUCUUCAAA-3′; human NBR1 (L-010522-00): 5′-GAGAACAAGUGGUUAACGA-3′, 5′-CCACAUGACAGUCCUUUAA-3′, 5′-GAACGUAUACUUCCCAUUG-3′, and 5′-AGAAGCCACUUGCACAUUA-3′; human OPTN (L-016269-00): 5′-GGGCUCAGAUGGAAGUUUA-3′, 5′-CCAUGAAGCUAAAUAAUCA-3′, 5′-CUUCGAACAUGAGGAGUUA-3′, and 5′-CUAAUGGCCUUGAGUCAUG-3′; human CALCOCO2/NDP52 (L-010637-00): 5′-GGAAACCCAUAUUCUGGUA-3′, 5′-GGAUUGGAUUGGCAUCUUU-3′, 5′-GGACGUCACAUGUCAUUAU-3′, and 5′-GGAAGACAACCCGUGAGUA-3′; and nontargeting control (D-001810-10): 5′-UGGUUUACAUGUCGACUAA-3′, 5′-UGGUUUACAUGUUGUGUGA-3′, 5′-UGGUUUACAUGUUUUCUGA-3′, and 5′-UGGUUUACAUGUUUUCCUA-3′.

The Amaxa Nucleofector device (Lonza) was used to electroporate cells using program T-024 and nucleofector kit V according to manufacturer's instructions.

Antibodies, immunoblotting, immunoprecipitation, and immunofluorescence

The following antibodies were used for immunoblotting: goat anti-ATG7 for human (sc-8668, 1:200; Santa Cruz Biotechnology, Inc.), rabbit anti-ATG12 for human (2010, 1:500; Cell Signaling), rabbit anti-ATG7 for mouse (2631, 1:500; Cell Signaling), rabbit anti-ATG 12 for mouse (2011, 1:500; Cell Signaling), guinea pig anti-p62/SQSTM1 (GP62-C, 1:1,000; Progen Biotechnik), mouse anti-NBR 1 (H00004077-A01, 1:500; Abnova), rabbit anti-OPTN (ab23666, 1:1,000; Abcam), rabbit anti-CALCOCO2/NDP52 (ab68588, 1:500; Abcam), mouse anti-GFP (390394, 1:500; Santa Cruz Biotechnology, Inc.), mouse anti-paxillin (610051, 1:1,000; BD Biosciences), mouse anti-FAK (610087, 1:500; BD Biosciences), mouse anti-vinculin (V9131, 1:1,000; Sigma-Aldrich), mouse anti-zyxin (H00007791-M01, 1:500; Abnova), mouse anti-TUBA (T6199, 1:5,000; Sigma Aldrich), and mouse anti-GAPDH (AB2302, 1:5,000; Millipore). A rabbit polyclonal antibody against MAP1LC3 has been previously described (Fung et al., 2008) and is now commercially available (ABC232, 1:1,000; Millipore).

For immunoblot analysis, cells were lysed in RIPA buffer (1% Triton X-100, 1% sodium deoxycholate, 0.1% SDS, 25 mM Tris, pH 7.6, and 150 mM NaCl) plus protease inhibitor cocktail (Sigma-Aldrich), 10 mM NaF, 10 mM β-glycerophosphate, 1 mM Na_3VO_4, 10 nM calyculin A, 0.5 mM PMSF, 10 µg/ml E64d, and 10 µg/ml pepstatin A. Lysates were freeze-thawed at –80°C, cleared by centrifugation for 30 min at 4°C, boiled in sample buffer, resolved by SDS-PAGE, and transferred to polyvinylidene fluoride membrane. Membranes were blocked for 1 h in 5% milk in PBS with 0.1% Tween 20, incubated in primary antibody overnight at 4°C, washed, incubated for 1 h at RT with HRP-conjugated goat secondary antibodies (1:5,000; Jackson ImmunoResearch Laboratories), washed, and visualized via enhanced chemiluminescence (Thermo Fisher Scientific).

For immunoprecipitation, cells expressing GFP or GFP-NBR1 were sparsely plated on fibronectin-coated (10 µg/ml in PBS) dishes and were lysed in nondenaturing lysis buffer (1% Triton X-100, 25 mM Tris HCl, pH 7.4, and 150 mM NaCl) plus protease inhibitor cocktail (Sigma-Aldrich), 10 mM N-ethylmaleimide, 10 mM NaF, 10 mM β-glycerophosphate, 1 mM Na_3VO_4, 10 nM calyculin A, 0.5 mM PMSF, 10 µg/ml E64d, and 10 µg/ml pepstatin A. Lysates were precleared with protein A/G beads (Santa Cruz Biotechnology, Inc.) and normal rabbit IgG (Santa Cruz Biotechnology, Inc.) at 4°C and incubated overnight with rabbit anti-GFP primary antibody (ab6556; Abcam; 1 µg/200–300 µg lysate) at 4°C. Immune complexes were captured by incubation with protein A/G beads for 4 h at 4°C and then washed six times with PBS plus inhibitors, eluted with sample buffer, and analyzed by immunoblotting. For immunoblot analysis of paxillin from anti-GFP immunoprecipitates, rat anti–mouse HRP TrueBlot (18-8817-33, 1:1,000; Rockland Immunochemicals) was used.

For immunofluorescence, mouse anti-paxillin (610619, 1:200; BD Biosciences) and rabbit anti-NBR1 (71703, 1:200; Novus) were used. Alexa Fluor 488–conjugated phalloidin (A12379, 1:200; Life Technologies) was used for imaging the F-actin cytoskeleton. Cells were fixed with 4% PFA for 20 min at RT, permeabilized with 0.5% Triton X-100 in PBS, rinsed with PBS-glycine, and blocked overnight at 4°C in blocking buffer (10% goat serum and 0.2% Triton X-100 in PBS). Cells were incubated with primary antibodies for 1 h at RT, washed, incubated with Alexa Fluor 488 or 594 goat secondary antibodies (1:500; Life Technologies) for 40 min at RT, washed, and mounted using Prolong Gold Anti-Fade mounting medium (Life Technologies).

Microscopy

For all live-cell imaging and static images of cells during wound healing, cells were imaged in the assay media described for scratch wound-healing migration assay. For cells expressing paxillin-mTurquoise, phenol red-free DMEM/F12 was used to prepare assay media. Fixed specimens for immunofluorescence and SIM were mounted with hard-set Prolong Gold Anti-Fade mounting medium for imaging. Fixed cells for cell spreading assays were imaged in PBS.

Static phase contrast and epifluorescence images were obtained at ambient temperature using an Axiovert 200 microscope (Carl Zeiss) with a 10× (NA, 0.25) or 20× (NA, 0.4) objective, Spot RT camera (Diagnostic Instruments), and mercury lamp (for ZsGreen). Images were acquired using MetaMorph software (v6.0; Molecular Devices). Phase-contrast microscopy time-lapse sequences were acquired on a TE 2000–inverted microscope stand (Nikon) with a CoolSNAP HQ2 scientific grade interline charge coupled device camera (Photometrics) and a 40× (NA, 0.6) objective (CFI Plan Fluor ELWD DM; Nikon) housed in an environmentally controlled chamber at 37°C. Microscope hardware and image acquisition were controlled by NIS-Elements software (Nikon).

Spinning disk confocal imaging was performed as previously described (Stehbens et al., 2014; Stehbens and Wittmann, 2014) using an environmentally controlled TI-inverted microscope stand (Nikon) equipped with a Borealis-modified Yokogawa CSU-X1 confocal head (Spectral Applied Research), solid-state 442-nm (for mTurquoise), 488-nm (for GFP, ZsGreen, and Alexa Fluor 488), 515-nm (for Venus), and 561-nm (for mCherry and Alexa Fluor 594) lasers, and a Clara cooled scientific-grade interline CCD camera (Andor) or a CoolSNAP MYO cooled scientific-grade CCD camera (Photometrics). Intracellular fluorescent-tagged protein dynamics in live cells were imaged at 37°C using a 60× (NA, 1.49; oil) objective (CFI Apochromat TIRF; Nikon), and immunofluorescence images were acquired at 37°C using a 100× (NA, 1.49; oil) objective (CFI Aprochromat; Nikon). Live-cell spreading of ZsGreen cells was imaged at 37°C using a 10× (NA, 0.45) objective (CFI Plan Apochromat; Nikon). TIRF microscopy of live cells was performed at 37°C on the same Nikon TI-inverted microscope stand equipped with a motorized TIRF illuminator (Nikon) and an iXon electron-multiplying CCD camera (Andor). TIRF images were acquired using a 100× objective

(NA, 1.49; oil), with 1.5× intermediate magnification. Microscope hardware was controlled with NIS-Elements.

Super-resolution SIM was performed on a Ti-E–inverted microscope stand (Nikon) with 488-nm (for GFP) and 561-nm (for mCherry) lasers and an iXon DU-897 electron multiplying CCD camera (Andor). Imaging was performed on fixed samples at ambient temperature using a 100× (NA, 1.49; oil) objective (CFI Aprochromat; Nikon). Microscope hardware was controlled with NIS-Elements.

For analysis of all microscopy images, raw image data were used. Details of image analysis for each experimental technique and image processing for presentation are described in the following sections.

Scratch-wound healing migration assay

For assessment of wound closure by different cell types, monolayers were grown to confluency and incubated in the following media: assay media supplemented with 5 ng/ml EGF for wild-type MCF10A cells, DMEM with 2% FBS, 50 ng/ml EGF, penicillin, and streptomycin for PyMT cells, and DMEM supplemented with 2% FBS, penicillin, and streptomycin for iBMK cells. The proliferation inhibitor mitomycin C (1 µg/ml) was added to the cultures during assays. Confluent monolayers were wounded using a 200-µl pipette tip, washed several times to remove cell debris, and imaged at time of wounding (0 h) and the indicated time points. Wound widths were determined using MetaMorph software and were taken as the mean of six to nine measurements across the wound; to account for differences in starting wound width, data are reported as the decrease in wound width calculated by subtracting the final width from the initial width.

For live-cell phase contrast imaging of migrating MCF10A-Ras cells, cells were grown to confluency on 3.5-cm glass bottom dishes (Mattek), incubated in assay media, and wounded. Image fields were randomly chosen along the length of the wound, and images were acquired every 3 min for 3 h. Single-cell tracking analysis was performed in NIS-Elements by randomly choosing one to two cells per image field and using the "Tracking" feature to manually track cell nucleoli (discerned as dark spots in the nucleus) for each frame over the time course; time and position data were then used to create single-cell migration paths and calculate migration speed as the total distance traveled divided by total time ($d/t_f - t_0$) for each cell over 3 h.

Cell-spreading assay

Coverslips in 24-well dishes and glass bottom six-well dishes (Mattek) were prepared by coating overnight at 4°C with 10 µg/ml fibronectin in PBS and then blocking with 1% BSA in DMEM/F12 for 30 min at 37°C. Subconfluent monolayers of MCF10A-Ras cells expressing ZsGreen were incubated overnight in assay media, harvested with fresh aliquots of 0.05% trypsin/EDTA diluted 1:1 with PBS, and sparsely plated in assay media. To synchronize attachment and initiation of spreading, plates were spun at 300 rpm in a swinging bucket rotor for 5 min immediately on plating cells. For live-cell confocal imaging of spreading, cells in six-well dishes were imaged every 5 min for 3 h. Cells on coverslips were incubated for 1 h, fixed in 4% PFA for 20 min at RT, and stored in PBS for imaging; epifluorescence images of fixed ZsGreen-expressing cells were used to quantify cell area using ImageJ (National Institutes of Health) by manually outlining cell borders. For each experiment, two coverslips per condition were plated, and four random fields per coverslip were imaged. All cells entirely present in each image field were measured.

FA size analysis

MCF10A-Ras cells were plated at confluency in assay media on coverslips coated with 10 µg/ml fibronectin, wounded, and fixed 4–6 h after wounding for anti-paxillin immunostaining. Confocal images of migrating cells were acquired randomly along the wound edge, and FAs at the leading edge of cells were manually outlined for area measurements using NIS-Elements. FAs from one to three cells were measured in each field, and the mean area of FAs per field was determined and plotted.

FA turnover assay and analysis

Analysis of dynamic FA turnover in live cells was performed as previously described (Stehbens et al., 2014; Stehbens and Wittmann, 2014). In brief, MCF10A-Ras cells expressing paxillin-mCherry were plated at confluency in assay media on 3.5-cm glass bottom dishes coated with 10 µg/ml fibronectin and wounded. 15–25 image fields were taken along the wound edge, and cells were imaged every 2–3 min for 1.5–3 h. For analysis, FAs were randomly chosen, and three to five FAs were measured per cell; only FAs that could be tracked completely from their appearance through disappearance were measured. To track FAs, the Bezier ROI tool was used to manually outline individual FAs and was redrawn in each frame as necessary over time if the FA significantly changed in size or location. The "Time Measurement" feature in NIS-Elements was used to generate fluorescence intensity data for each tracked FA, and background intensity was similarly determined using a duplicated region of interest placed adjacent to the FA. Background corrected intensity data were smoothed with a three-frame running mean and plotted against time. Smoothed fluorescence intensity curve plots were used to calculate FA assembly rate constant, disassembly rate constant, and lifetime by curve fitting in Excel (Microsoft). Assembly was determined by curve fitting the initial portion of the intensity plot during which fluorescence intensity steadily increases (when the FA is assembling) with a logistic function (Fig. 2 B, green line). Disassembly was determined by curve fitting the latter portion of the intensity plot when fluorescence intensity is decreasing (FA disassembly) with an exponential function (Fig. 2 B, red line). Rate constants for each parameter were obtained from these functions for each FA. The assembly and disassembly curve fits were also used to calculate FA lifetime, the time during which fluorescence intensity remained above half of the maximum intensity value (Fig. 2 B, double black arrow).

Analysis of GFP-LC3 and GFP-NBR1 targeting to FAs in live cells

MCF10A-Ras cells coexpressing GFP-LC3 and paxillin-mCherry were imaged every 3 min during migration as described under FA turnover assay and analysis. For enumeration of GFP-LC3 targeting to FAs, 5–10 FAs were first randomly chosen per cell independent of the GFP channel, and then, the number of GFP-LC3 vesicles that associated with each FA was counted. Note that targeting was strictly defined as observable physical contact of GFP-LC3 vesicles with FAs (Fig. 4 B). Multiple targeting events were counted if the FA was targeted more than once over its lifetime or by multiple vesicles at the same time. Then, FAs were tracked and measured as described in FA turnover assay and analysis for generation of paxillin-mCherry fluorescence intensity plots to delineate assembly, stability, and disassembly phases of each targeted FA to determine the phase during which GFP-LC3 targeting events occurred. Qualitative live-cell analysis of GFP-LC3 association with dynamic FAs during spreading was performed by imaging cells within 30 min of plating at 1-min intervals.

For analysis of enrichment of GFP-LC3 at FAs, three random frames per time lapse were chosen for each cell, and GFP-LC3 puncta at FAs and in non-FA areas were enumerated in the leading edge region. Total FA area and non-FA areas were manually measured for the leading edge, and the number of puncta per square micrometer FA or non-FA area was determined by dividing the total number of puncta for that region by the total area for that region. GFP-NBR1 enrichment at FAs was quantified in the same manner.

Localization of mCherry-tagged FA proteins to autophagosomes

For two-color imaging of paxillin and autophagosomes, MCF10A-Ras cells stably coexpressing GFP-LC3 and paxillin-mCherry as described for analysis of GFP-LC3 targeting to FAs were used. For two-color imaging of vinculin or zyxin and autophagosomes, MCF10A-Ras cells stably expressing GFP-LC3 were electroporated using the Amaxa nucleofector device as described for RNA interference with mCherry-vinculin or zyxin-mCherry. Cells were plated, wounded, and imaged by spinning disk confocal microscopy as described for FA turnover and analysis, and GFP/mCherry double-positive puncta were identified in migrating cells.

Analysis of Venus-LC3 and mCherry-NBR1 colocalization at FAs

MCF10A-Ras cells stably coexpressing paxillin-mTurquoise, Venus-LC3, and mCherry-NBR1 were plated and imaged by spinning disk confocal microscopy after wounding as described in FA turnover assay and analysis. For analysis, three random frames per time lapse were chosen for each cell. FA-associated Venus-LC3 puncta were identified using the paxillin-mTurquoise and Venus-LC3 channels. Then, the Venus-LC3 and mCherry-NBR1 channels were used to count the number of FA-associated Venus-LC3 puncta that were also mCherry-NBR1 positive.

Image processing

All image analysis was performed on raw image data; however, for presentation purposes, images were processed using established methods (Stehbens et al., 2014). In NIS-Elements, 14-bit spinning disk confocal microscopy time-lapse sequences of paxillin-mCherry were corrected for photobleaching over time using the "Equalize Intensity in Time" tool, and reduction of pixel noise and enhancement of contrast were performed using a low-pass filter and unsharp mask, respectively. Images were then linearly adjusted as needed for brightness and contrast and converted to 8 bit. "Complement Colors" was used to contrast invert images for visualization of black FAs on a white background. Throughout the figures, leading edge inset areas were cropped and rotated for closer visualization of FA dynamics.

To generate two-color black/magenta images as previously described (Stehbens et al., 2014) of GFP-LC3 and paxillin-mCherry or GFP-NBR1 and paxillin-mCherry, the GFP and mCherry channels were first separated and processed individually to 8-bit images as detailed for single-color time-lapse sequences of paxillin-mCherry. Next, the images were added using ND Image Arithmetics: GFP + mCherry, and subsequently combined by merging channels (red: GFP , green: GFP + mCherry (from ND Arithmetics), and blue: GFP). The merged image was then contrast inverted using "Complement Colors" to create black/magenta overlays with magenta FAs and black vesicles on a white background.

Two-color immunofluorescence (Alexa Fluor 488/Alexa Fluor 594) and live-cell (GFP/mCherry) images were processed to 8 bit as described for single-color time-lapse sequences of paxillin-mCherry, and green/magenta overlays were created in NIS-Elements using merge channels (red: 561 nm, green: 488 nm, and blue: 561 nm). Three-color (mTurquoise/Venus/mCherry) live-cell images were also processed as described for two-color images in NIS-Elements. Finally, both phase contrast and epifluorescence images were linearly brightness and contrast adjusted to better discern cell bodies and outlines in MetaMorph or ImageJ.

Statistical analysis

All statistical analyses were performed using GraphPad Prism 6 (GraphPad Software). The normality of the distribution of datasets was determined by a Shapiro–Wilk normality test ($P < 0.05$, indicating a non-normal distribution); for datasets in which the sample size was not large enough ($n \leq 6$) for determination of normality, a normal distribution was assumed. For normal distributions, groups were compared using unpaired *t* test or one-way analysis of variance followed by Tukey post-hoc test for multiple comparisons. For nonparametric statistics, a Mann-Whitney test or Kruskall-Wallis test followed by Dunn's post-hoc test for multiple comparisons was used. $P < 0.05$ was considered to be significant for all tests.

Online supplemental materials

Fig. S1 shows that inhibition of autophagy caused by loss of ATGs impairs migration and leads to enlarged FAs in multiple epithelial cell types. Fig. S2 shows SIM and TIRF imaging of autophagosomes at FAs and presence of mCherry-tagged FA proteins at autophagosomes. Fig. S3 shows validation of RNA interference against autophagy cargo receptors, no changes in basal autophagic flux with NBR1 depletion, and localization of NBR1 to FAs. Fig. S4 shows that loss of NBR1 leads to enhanced cell spreading. Fig. S5 shows interaction of GFP-NBR 1 with endogenous FA proteins and representative paxillin-mCherry time-lapse sequences of cells expressing GFP, GFP-NBR1, GFP-NBR 1 ΔLIR, or GFP-NBR1 ΔUBA. Video 1 shows migration of autophagy-inhibited cells. Videos 2 and 3 show FA dynamics upon autophagy inhibition in migrating cells expressing paxillin-mCherry. Video 4 shows a migrating cell expressing GFP-LC3 and paxillin-mCherry. Videos 5 and 6 show FA dynamics in a migrating cell expressing GFP -LC3 and paxillin-mCherry. Videos 7 and 8 show FA dynamics upon depletion of NBR1 in migrating cells expressing paxillin-mCherry. Video 9 shows the leading edge of a migrating cell expressing GFP -NBR1 and paxillin-mCherry. Online supplemental material is available at http://www.jcb.org/cgi/content/full/jcb.201503075/DC1.

Acknowledgments

Confocal and TIRF microscopy and image analysis were performed in the Biological Imaging Development Center at University of California, San Francisco (UCSF). SIM was performed in the Nikon Imaging Center at UCSF. We thank D. Sheppard and N. Reed for advice on spreading adhesion assays.

Grant support to J. Debnath includes National Institutes of Health (CA126792 and CA188404), Department of Defense Breast Cancer Research Program (W81XWH-11-1-0130 and W81XWH-12-1-0505), and Samuel Waxman Cancer Research Foundation. Grant support to T. Wittmann includes National Institutes of Health (GM079139 and S10 RR26758). C.M. Kenific was supported by a National Institutes of Health Predoctoral Fellowship (F31CA167905), and J. Goldsmith is supported by a National Science Foundation Graduate Student Fellowship (DGE-1144247).

The authors declare no competing financial interests.

Author contributions: C.M. Kenific and J. Debnath conceived the study. C.M. Kenific and J. Debnath designed the experiments with input from S.J. Stehbens and T. Wittmann. C.M. Kenific, J. Goldsmith, A.M. Leidal, N. Faure, and J. Ye performed experiments. C.M. Kenific and J. Debnath analyzed the data. S.J. Stehbens and T. Wittmann created analytical tools crucial for quantitative assessment of dynamic FA turnover. C.M. Kenific and J. Debnath wrote the manuscript, with input from the other authors.

Submitted: 16 March 2015
Accepted: 19 January 2016

References

Birgisdottir, A.B., T. Lamark, and T. Johansen. 2013. The LIR motif - crucial for selective autophagy. *J. Cell Sci.* 126:3237–3247. http://dx.doi.org/10.1242/jcs.12612

Campeau, E., V.E. Ruhl, F. Rodier, C.L. Smith, B.L. Rahmberg, J.O. Fuss, J. Campisi, P. Yaswen, P.K. Cooper, and P.D. Kaufman. 2009. A versatile viral system for expression and depletion of proteins in mammalian cells. *PLoS One.* 4:e6529. http://dx.doi.org/10.1371/journal.pone.0006529

Cavalcanti-Adam, E.A., T. Volberg, A. Micoulet, H. Kessler, B. Geiger, and J.P. Spatz. 2007. Cell spreading and focal adhesion dynamics are regulated by spacing of integrin ligands. *Biophys. J.* 92:2964–2974. http://dx.doi.org/10.1529/biophysj.106.089730

Chan, K.T., D.A. Bennin, and A. Huttenlocher. 2010. Regulation of adhesion dynamics by calpain-mediated proteolysis of focal adhesion kinase (FAK). *J. Biol. Chem.* 285:11418–11426. http://dx.doi.org/10.1074/jbc.M109.090746

Chao, W.T., and J. Kunz. 2009. Focal adhesion disassembly requires clathrin-dependent endocytosis of integrins. *FEBS Lett.* 583:1337–1343. http://dx.doi.org/10.1016/j.febslet.2009.03.037

Cortesio, C.L., L.R. Boateng, T.M. Piazza, D.A. Bennin, and A. Huttenlocher. 2011. Calpain-mediated proteolysis of paxillin negatively regulates focal adhesion dynamics and cell migration. *J. Biol. Chem.* 286:9998–10006. http://dx.doi.org/10.1074/jbc.M110.187294

Debnath, J., S.K. Muthuswamy, and J.S. Brugge. 2003. Morphogenesis and oncogenesis of MCF-10A mammary epithelial acini grown in three-dimensional basement membrane cultures. *Methods.* 30:256–268. http://dx.doi.org/10.1016/S1046-2023(03)00032-X

Deng, S., and C. Huang. 2014. E3 ubiquitin ligases in regulating stress fiber, lamellipodium, and focal adhesion dynamics. *Cell Adhes. Migr.* 8:49–54. http://dx.doi.org/10.4161/cam.27480

Deosaran, E., K.B. Larsen, R. Hua, G. Sargent, Y. Wang, S. Kim, T. Lamark, M. Jauregui, K. Law, J. Lippincott-Schwartz, et al. 2013. NBR1 acts as an autophagy receptor for peroxisomes. *J. Cell Sci.* 126:939–952. http://dx.doi.org/10.1242/jcs.114819

DiMilla, P.A., K. Barbee, and D.A. Lauffenburger. 1991. Mathematical model for the effects of adhesion and mechanics on cell migration speed. *Biophys. J.* 60:15–37. http://dx.doi.org/10.1016/S0006-3495(91)82027-6

DiMilla, P.A., J.A. Stone, J.A. Quinn, S.M. Albelda, and D.A. Lauffenburger. 1993. Maximal migration of human smooth muscle cells on fibronectin and type IV collagen occurs at an intermediate attachment strength. *J. Cell Biol.* 122:729–737. http://dx.doi.org/10.1083/jcb.122.3.729

Dowdle, W.E., B. Nyfeler, J. Nagel, R.A. Elling, S. Liu, E. Triantafellow, S. Menon, Z. Wang, A. Honda, G. Pardee, et al. 2014. Selective VPS34 inhibitor blocks autophagy and uncovers a role for NCOA4 in ferritin degradation and iron homeostasis in vivo. *Nat. Cell Biol.* 16:1069–1079. http://dx.doi.org/10.1038/ncb3053

Dull, T., R. Zufferey, M. Kelly, R.J. Mandel, M. Nguyen, D. Trono, and L. Naldini. 1998. A third-generation lentivirus vector with a conditional packaging system. *J. Virol.* 72:8463–8471.

Ezratty, E.J., M.A. Partridge, and G.G. Gundersen. 2005. Microtubule-induced focal adhesion disassembly is mediated by dynamin and focal adhesion kinase. *Nat. Cell Biol.* 7:581–590. http://dx.doi.org/10.1038/ncb1262

Ezratty, E.J., C. Bertaux, E.E. Marcantonio, and G.G. Gundersen. 2009. Clathrin mediates integrin endocytosis for focal adhesion disassembly in migrating cells. *J. Cell Biol.* 187:733–747. http://dx.doi.org/10.1083/jcb.200904054

Feng, Y., D. He, Z. Yao, and D.J. Klionsky. 2014. The machinery of macroautophagy. *Cell Res.* 24:24–41. http://dx.doi.org/10.1038/cr.2013.168

Franco, S.J., M.A. Rodgers, B.J. Perrin, J. Han, D.A. Bennin, D.R. Critchley, and A. Huttenlocher. 2004. Calpain-mediated proteolysis of talin regulates adhesion dynamics. *Nat. Cell Biol.* 6:977–983. http://dx.doi.org/10.1038/ncb1175

Friedl, P., and K. Wolf. 2010. Plasticity of cell migration: a multiscale tuning model. *J. Cell Biol.* 188:11–19. http://dx.doi.org/10.1083/jcb.200909003

Fung, C., R. Lock, S. Gao, E. Salas, and J. Debnath. 2008. Induction of autophagy during extracellular matrix detachment promotes cell survival. *Mol. Biol. Cell.* 19:797–806. http://dx.doi.org/10.1091/mbc.E07-10-1092

Galavotti, S., S. Bartesaghi, D. Faccenda, M. Shaked-Rabi, S. Sanzone, A. McEvoy, D. Dinsdale, F. Condorelli, S. Brandner, M. Campanella, et al. 2013. The autophagy-associated factors DRAM1 and p62 regulate cell migration and invasion in glioblastoma stem cells. *Oncogene.* 32:699–712. http://dx.doi.org/10.1038/onc.2012.111

Gardel, M.L., I.C. Schneider, Y. Aratyn-Schaus, and C.M. Waterman. 2010. Mechanical integration of actin and adhesion dynamics in cell migration. *Annu. Rev. Cell Dev. Biol.* 26:315–333. http://dx.doi.org/10.1146/annurev.cellbio.011209.122036

Geiger, B., and K.M. Yamada. 2011. Molecular architecture and function of matrix adhesions. *Cold Spring Harb. Perspect. Biol.* 3:a005033. http://dx.doi.org/10.1101/cshperspect.a005033

Geiger, T., and R. Zaidel-Bar. 2012. Opening the floodgates: proteomics and the integrin adhesome. *Curr. Opin. Cell Biol.* 24:562–568. http://dx.doi.org/10.1016/j.ceb.2012.05.004

Gupton, S.L., and C.M. Waterman-Storer. 2006. Spatiotemporal feedback between actomyosin and focal-adhesion systems optimizes rapid cell migration. *Cell.* 125:1361–1374. http://dx.doi.org/10.1016/j.cell.2006.05.029

Hu, K., L. Ji, K.T. Applegate, G. Danuser, and C.M. Waterman-Storer. 2007. Differential transmission of actin motion within focal adhesions. *Science.* 315:111–115. http://dx.doi.org/10.1126/science.1135085

Huttenlocher, A., M.H. Ginsberg, and A.F. Horwitz. 1996. Modulation of cell migration by integrin-mediated cytoskeletal linkages and ligand-binding affinity. *J. Cell Biol.* 134:1551–1562. http://dx.doi.org/10.1083/jcb.134.6.1551

Itakura, E., and N. Mizushima. 2011. p62 Targeting to the autophagosome formation site requires self-oligomerization but not LC3 binding. *J. Cell Biol.* 192:17–27. http://dx.doi.org/10.1083/jcb.201009067

Johansen, T., and T. Lamark. 2011. Selective autophagy mediated by autophagic adapter proteins. *Autophagy.* 7:279–296. http://dx.doi.org/10.4161/auto.7.3.14487

Kirkin, V., T. Lamark, Y.S. Sou, G. Bjørkøy, J.L. Nunn, J.A. Bruun, E. Shvets, D.G. McEwan, T.H. Clausen, P. Wild, et al. 2009. A role for NBR1 in autophagosomal degradation of ubiquitinated substrates. *Mol. Cell.* 33:505–516. http://dx.doi.org/10.1016/j.molcel.2009.01.020

Kitamura, T., Y. Koshino, F. Shibata, T. Oki, H. Nakajima, T. Nosaka, and H. Kumagai. 2003. Retrovirus-mediated gene transfer and expression cloning: powerful tools in functional genomics. *Exp. Hematol.* 31:1007–1014. http://dx.doi.org/10.1016/S0301-472X(03)00260-1

Koyama-Honda, I., E. Itakura, T.K. Fujiwara, and N. Mizushima. 2013. Temporal analysis of recruitment of mammalian ATG proteins to the autophagosome formation site. *Autophagy.* 9:1491–1499. http://dx.doi.org/10.4161/auto.25529

Kraft, C., M. Peter, and K. Hofmann. 2010. Selective autophagy: ubiquitin-mediated recognition and beyond. *Nat. Cell Biol.* 12:836–841. http://dx.doi.org/10.1038/ncb0910-836

Kuo, T.C., C.T. Chen, D. Baron, T.T. Onder, S. Loewer, S. Almeida, C.M. Weismann, P. Xu, J.M. Houghton, F.B. Gao, et al. 2011. Midbody accumulation through evasion of autophagy contributes to cellular reprogramming and tumorigenicity. *Nat. Cell Biol.* 13:1214–1223. http://dx.doi.org/10.1038/ncb2332

Lange, S., F. Xiang, A. Yakovenko, A. Vihola, P. Hackman, E. Rostkova, J. Kristensen, B. Brandmeier, G. Franzen, B. Hedberg, et al. 2005. The kinase domain of titin controls muscle gene expression and protein turnover. *Science.* 308:1599–1603. http://dx.doi.org/10.1126/science.1110463

Lock, R., C.M. Kenific, A.M. Leidal, E. Salas, and J. Debnath. 2014. Autophagy-dependent production of secreted factors facilitates oncogenic RAS-driven invasion. *Cancer Discov.* 4:466–479. http://dx.doi.org/10.1158/2159-8290.CD-13-0841

Mancias, J.D., X. Wang, S.P. Gygi, J.W. Harper, and A.C. Kimmelman. 2014. Quantitative proteomics identifies NCOA4 as the cargo receptor mediating ferritinophagy. *Nature.* 509:105–109. http://dx.doi.org/10.1038/nature13148

Martin, M.D., K.J. Carter, S.R. Jean-Philippe, M. Chang, S. Mobashery, S. Thiolloy, C.C. Lynch, L.M. Matrisian, and B. Fingleton. 2008. Effect of ablation or inhibition of stromal matrix metalloproteinase-9 on lung metastasis in a breast cancer model is dependent on genetic background. *Cancer Res.* 68:6251–6259. http://dx.doi.org/10.1158/0008-5472.CAN-08-0537

Mathew, R., K. Degenhardt, L. Haramaty, C.M. Karp, and E. White. 2008. Immortalized mouse epithelial cell models to study the role of apoptosis in cancer. *Methods Enzymol.* 446:77–106. http://dx.doi.org/10.1016/S0076-6879(08)01605-4

Meenderink, L.M., L.M. Ryzhova, D.M. Donato, D.F. Gochberg, I. Kaverina, and S.K. Hanks. 2010. P130Cas Src-binding and substrate domains have distinct roles in sustaining focal adhesion disassembly and promoting cell migration. *PLoS One.* 5:e13412. http://dx.doi.org/10.1371/journal.pone.0013412

Müller, S., I. Kursula, P. Zou, and M. Wilmanns. 2006. Crystal structure of the PB1 domain of NBR1. *FEBS Lett.* 580:341–344. http://dx.doi.org/10.1016/j.febslet.2005.12.021

Murrow, L., and J. Debnath. 2013. Autophagy as a stress-response and quality-control mechanism: implications for cell injury and human disease. *Annu. Rev. Pathol.* 8:105–137. http://dx.doi.org/10.1146/annurev-pathol-020712-163918

Ory, D.S., B.A. Neugeboren, and R.C. Mulligan. 1996. A stable human-derived packaging cell line for production of high titer retrovirus/vesicular stomatitis virus G pseudotypes. *Proc. Natl. Acad. Sci. USA.* 93:11400–11406. http://dx.doi.org/10.1073/pnas.93.21.11400

Palecek, S.P., J.C. Loftus, M.H. Ginsberg, D.A. Lauffenburger, and A.F. Horwitz. 1997. Integrin-ligand binding properties govern cell migration speed through cell-substratum adhesiveness. *Nature.* 385:537–540. http://dx.doi.org/10.1038/385537a0

Pohl, C., and S. Jentsch. 2009. Midbody ring disposal by autophagy is a post-abscission event of cytokinesis. *Nat. Cell Biol.* 11:65–70. http://dx.doi.org/10.1038/ncb1813

Ridley, A.J., M.A. Schwartz, K. Burridge, R.A. Firtel, M.H. Ginsberg, G. Borisy, J.T. Parsons, and A.R. Horwitz. 2003. Cell migration: integrating signals from front to back. *Science.* 302:1704–1709. http://dx.doi.org/10.1126/science.1092053

Rogov, V., V. Dötsch, T. Johansen, and V. Kirkin. 2014. Interactions between autophagy receptors and ubiquitin-like proteins form the molecular basis for selective autophagy. *Mol. Cell.* 53:167–178. http://dx.doi.org/10.1016/j.molcel.2013.12.014

Schiller, H.B., and R. Fässler. 2013. Mechanosensitivity and compositional dynamics of cell-matrix adhesions. *EMBO Rep.* 14:509–519. http://dx.doi.org/10.1038/embor.2013.49

Shi, F., and J. Sottile. 2011. MT1-MMP regulates the turnover and endocytosis of extracellular matrix fibronectin. *J. Cell Sci.* 124:4039–4050. http://dx.doi.org/10.1242/jcs.087858

Stehbens, S.J., and T. Wittmann. 2014. Analysis of focal adhesion turnover: a quantitative live-cell imaging example. *Methods Cell Biol.* 123:335–346. http://dx.doi.org/10.1016/B978-0-12-420138-5.00018-5

Stehbens, S.J., M. Paszek, H. Pemble, A. Ettinger, S. Gierke, and T. Wittmann. 2014. CLASPs link focal-adhesion-associated microtubule capture to localized exocytosis and adhesion site turnover. *Nat. Cell Biol.* 16:561–573. http://dx.doi.org/10.1038/ncb2975

Tuloup-Minguez, V., A. Hamaï, A. Greffard, V. Nicolas, P. Codogno, and J. Botti. 2013. Autophagy modulates cell migration and β1 integrin membrane recycling. *Cell Cycle.* 12:3317–3328. http://dx.doi.org/10.4161/cc.26298

Waters, S., K. Marchbank, E. Solomon, C. Whitehouse, and M. Gautel. 2009. Interactions with LC3 and polyubiquitin chains link nbr1 to autophagic protein turnover. *FEBS Lett.* 583:1846–1852. http://dx.doi.org/10.1016/j.febslet.2009.04.049

Webb, D.J., K. Donais, L.A. Whitmore, S.M. Thomas, C.E. Turner, J.T. Parsons, and A.F. Horwitz. 2004. FAK-Src signalling through paxillin, ERK and MLCK regulates adhesion disassembly. *Nat. Cell Biol.* 6:154–161. http://dx.doi.org/10.1038/ncb1094

Welm, B.E., G.J. Dijkgraaf, A.S. Bledau, A.L. Welm, and Z. Werb. 2008. Lentiviral transduction of mammary stem cells for analysis of gene function during development and cancer. *Cell Stem Cell.* 2:90–102. http://dx.doi.org/10.1016/j.stem.2007.10.002

Whitehouse, C., J. Chambers, K. Howe, M. Cobourne, P. Sharpe, and E. Solomon. 2002. NBR1 interacts with fasciculation and elongation protein zeta-1 (FEZ1) and calcium and integrin binding protein (CIB) and shows developmentally restricted expression in the neural tube. *Eur. J. Biochem.* 269:538–545. http://dx.doi.org/10.1046/j.0014-2956.2001.02681.x

Winograd-Katz, S.E., R. Fässler, B. Geiger, and K.R. Legate. 2014. The integrin adhesome: from genes and proteins to human disease. *Nat. Rev. Mol. Cell Biol.* 15:273–288. http://dx.doi.org/10.1038/nrm3769

Wolfenson, H., I. Lavelin, and B. Geiger. 2013. Dynamic regulation of the structure and functions of integrin adhesions. *Dev. Cell.* 24:447–458. http://dx.doi.org/10.1016/j.devcel.2013.02.012

Zhan, Z., X. Xie, H. Cao, X. Zhou, X.D. Zhang, H. Fan, and Z. Liu. 2014. Autophagy facilitates TLR4- and TLR3-triggered migration and invasion of lung cancer cells through the promotion of TRAF6 ubiquitination. *Autophagy.* 10:257–268. http://dx.doi.org/10.4161/auto.27162